

Research Article

Tribology Characteristics of Ultrasonic Impact Treated Co-Based L-605 Superalloy

R. Nemati¹, R. Taghiabadi^{1*}, M. Saghafi Yazdi¹ and S. Amini²¹ Department of Metallurgy and Materials Science, Imam Khomeini International University, Qazvin, Iran² Faculty of Mechanical Engineering, Department of Mechanical Engineering, Manufacturing and Production, University of Kashan, Kashan, Iran

ARTICLE INFO

Article history:

Received 30 January 2025

Reviewed 1 March 2025

Revised 3 March 2025

Accepted 10 March 2025

Keywords:

L-605 alloy

Ultrasonic impact treatment

Sliding wear

Friction

Tribology

Please cite this article as:

Nemati, R., Taghiabadi, R., Saghafi Yazdi, M., & Amini, S. (2025). Tribology characteristics of ultrasonic impact treated Co-based L-605 superalloy. *Iranian Journal of Materials Forming*, 12(1), 37-50. <https://doi.org/10.22099/IJMF.2025.52344.1324>

ABSTRACT

This study investigates the effect of ultrasonic impact treatment (UIT) on the surface structure, microhardness, and tribological behavior of L-605 superalloy. The surface of the samples was impacted by a high-frequency (20 kHz) spherical tungsten carbide tool for one, two, three, and five passes, using a feed rate of 0.08 mm/min, vibration amplitude of 28 %, and static pressure of 0.1 MPa. Results showed that UIT significantly deformed the surface microstructure and enhanced surface microhardness, primarily due to work hardening, strain-induced martensitic transformation, and ultrafine grain formation. A single UIT pass notably improved wear resistance and reduced the friction coefficient. Compared to the annealed alloy, the one-pass UITED samples showed wear rate reductions of 74%, 70%, 68%, and 64% under loads of 5, 10, 25, and 75 N, respectively. The average friction coefficient also dropped by up to 80% at 10 N and 74% at 75 N. Additional UIT passes resulted in marginal microhardness improvement, likely due to strain hardening saturation in the surface layers.

© Shiraz University, Shiraz, Iran, 2025

1. Introduction

L-605, a heat-resistant Co-based superalloy, exhibits excellent mechanical properties, outstanding corrosion resistance, and good biocompatibility. These attributes make it a widely used material in military applications, gas turbines, surgical implants, and heart stents [1, 2]. However, its practical use is often challenged by surface-

related issues such as wear, corrosion and fatigue, which can lead to premature component failure and significant human and financial losses. These degradation phenomena typically originate at the surface and are strongly influenced by the material's surface properties. To address these challenges, various surface modification techniques, such as chemical and

* Corresponding author

E-mail address: taghiabadi@ikiu.ac.ir (R. Taghiabadi)<https://doi.org/10.22099/IJMF.2025.52344.1324>

electrochemical treatments, ion implantation, and laser processing, have been developed to enhance surface performance [3, 4].

L-605 is known for undergoing strain-induced phase transformation and can be strengthened through cold working [5]. As such, surface severe plastic deformation (S²PD) processes are promising approaches for improving the surface mechanical properties of this alloy. Numerous studies have explored the effect of S²PD methods on the surface characteristics of Co-based alloys; including peening-based techniques [6] and various types of burnishing processes [7]. Another emerging group of S²PD techniques involves the use of ultrasound waves, such as ultrasonic peening treatment (UPT), ultrasonic shot peening (USP) and ultrasonic impact treatment (UIT) [8-10]. These methods have recently attracted growing attention from researchers.

Among them, UIT stands out as a simple, safe, and efficient process. In UIT, a transducer converts electrical energy into high-frequency mechanical vibrations, which induce severe plastic deformation in the surface layers of the material. This localized deformation modifies the surface microstructure and enhances mechanical properties [5, 11]. The positive impacts of UIT on the surface microstructure and properties of alloys have been widely reported. For instance, Ansarian et al. [12], found that UIT increased surface hardness, promoted compressive residual stress, and enhanced the tribological behavior of laser powder bed fused (L-PBFed) commercially pure titanium (CP-Ti). Similarly, Karimi et al. [13] reported improved wear and friction performance in 1.7225 steel treated with UIT. The technique has also shown promising results in enhancing the tribological behavior of additively-manufactured CoCrMo alloys [14]. Lesyk et al. [15] compared several S²PD processes, including shot peening, barrel finishing, USP, and UIT, on L-PBFed Inconel 718, and found that UIT resulted in the most significant increase in surface hardness, up to 50%. Pennin et al. [16] highlighted UIT's grain-refining effect on the surface microstructure of CP-Ti. Wang et al. [17] demonstrated enhanced in Ti-6Al-4V alloy produced by laser metal deposition after layer-by-layer UIT. Their study reported that the yield

strength and ultimate tensile strength were improved by about 41% and 37 %, respectively, along with a transition from ductile to brittle fracture behavior. This was attributed to curved grain boundaries (nanostructure formation, and Hall-petch strengthening mechanisms. Amanov et al. investigated the ultrasonic nanocrystal surface modification (UNSM) process on the 316L stainless steel observing a reduction in wear rate from 4.2×10^{-4} to 3.3×10^{-4} mm³/Nm due to a shift from adhesive to abrasive wear mechanisms [18]. In another study, UNSM was shown to enhance the wear resistance of an additively manufactured CoCrMo alloy tested against AISI 5100 bearing steel balls, with the wear rate decreasing from 5.47×10^{-12} to 1.24×10^{-12} mm³/Nm following ultrasonic treatment [19].

Despite the proven effectiveness of UIT in modifying surface microstructure and enhancing the mechanical properties of various engineering alloys, a review of the literature reveals that limited attention has been given to its effect on the tribological performance of the L-605 superalloy. Therefore, the present study aims to investigate the influence of UIT pass number on the tribological properties of the L-605 superalloy.

2. Experimental Procedure

L-605 alloy sheets were fabricated by first melting the primary ingots in a vacuum induction melting (VIM) furnace, followed by electro-slag remelting (ESR). The remelted ingots were then hot rolled and subjected to solution annealing at 1180 °C, for two hours, followed by water quenching. The chemical composition of the alloy sheets, determined via atomic emission spectrometry, is presented in Table 1.

Table 1. Chemical composition of L605 alloy (wt.%)

Co	Cr	W	Ni	Fe
Base	19.46	14.1	10.14	3.67
Mn	Si	C	P	S
1.07	0.18	0.06	0.008	0.001

Primary samples, approximately 30 mm in length, 30 mm in width, and 7 mm in thickness were prepared by wire electrical discharge machining. Prior to UIT, the samples were annealed at 1200 °C for 0.5 hours in a

vacuum furnace and subsequently quenched to room temperature using argon gas. The annealed samples were then manually polished with 1200-grit SiC abrasive paper to ensure a consistent surface finish. UIT was performed using an MPA-3kW ultrasonic generator. The experimental setup for the UIT process is illustrated in Fig. 1(a-b). The main components of the UIT system included a piezoelectric transducer, a booster (used to amplify ultrasonic vibrations), an ultrasonic generator, and a horn (for transmitting the intensified vibrations to the tool). A spherically tipped tungsten carbide–cobalt (WC–Co) tool with a diameter of 10 mm was mounted at the end of the horn. An air compressor provided the necessary static load during the UIT process.

High-frequency ultrasonic vibration (20 kHz) was applied under a fixed static pressure of approximately 0.1 MPa, resulting in significant surface deformation of the samples, as illustrated in Fig. 1(c). The UIT process was carried out at room temperature with a spindle speed of 45 rpm, a feed rate of $0.08 \text{ mm}\cdot\text{rev}^{-1}$, and tool vibration amplitudes of 10 %, 28 %, and 50 %. Treatments were performed with one, two, three, and five passes. Based on preliminary testing, a vibration amplitude of 28 % was identified as optimal and was used for the subsequent experiments. Additional details regarding the UIT process can be found in [20].

Standard metallographic procedures were followed for surface preparation of experimental samples. The prepared surfaces were chemically etched for 40 seconds using a solution consisting of 20 mL HCL-1 mL H_2O_2 . Microstructure analysis was conducted using an Examet

Union 81892 OSK optical microscope (OM). To further examine the morphology and chemical composition of worn surfaces, a MIRA3 TESCAN scanning electron microscope (SEM) equipped with an energy-dispersive spectroscopy (EDS) detector was employed. High-resolution transmission electron microscopy (HRTEM) was also performed using an TECNAI F20 microscope equipped with a field emission gun operating at 200 kV.

Microhardness measurements were conducted using a SHAAB Model MS microhardness tester, following ASTM E384 standards. An applied load of 100 g and a dwell time of 10 seconds were used for all measurements. Nanoindentation tests were performed using Hysitron TriboScope® Nanomechanical instrument with a calibrated Berkovich diamond indenter. The tests were conducted under a peak load of $7,000 \mu\text{N}$ and a dwell time of 10 seconds, following calibration procedures outlined in the instrument's user manual. X-ray diffraction (XRD) analysis was performed using a copper cathode lamp with $\text{K}\alpha_1$ radiation (wavelength = 1.54060 \AA). The scanning range was set to $2\theta = 0.02^\circ$, with a scan time of 0.8 seconds per step. Room temperature sliding wear tests were conducted using a TR-20 DUCOM tribometer in a pin-on-disk configuration. Tests were performed over a sliding distance of 1000 m at a constant sliding speed of 0.2 m/s under applied normal loads of 5, 10, 25, and 75 N. Cubic flat-end pins with dimensions of $6 \times 5 \times 5 \text{ mm}$ were utilized against an alumina disk. Prior to each test, the samples were ultrasonically cleaned in acetone.

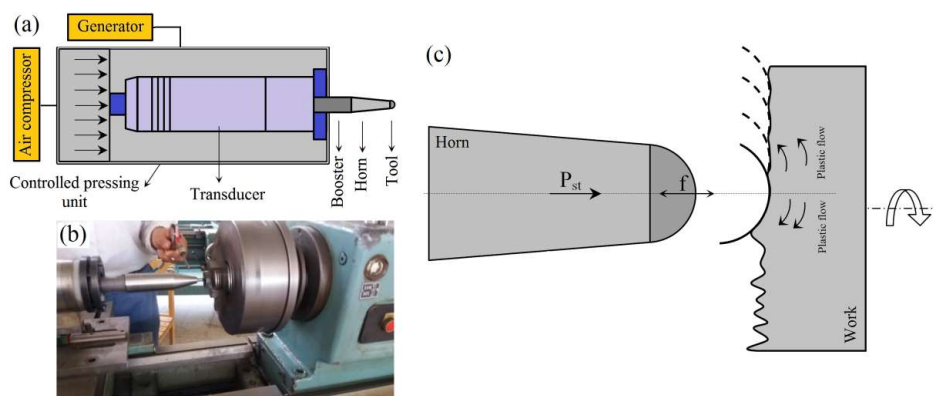


Fig. 1. (a) Schematic diagram of the UIT configuration setup, (b) experimental apparatus used for performing UIT, and (c) schematic close-up view of the tool tip illustrating its interaction with the sample surface during the treatment process.

The wear rate was calculated as the mass of material removed divided by the total sliding distance, while the specific wear rate was defined as the wear mass loss per unit distance per unit load.

3. Results and Discussion

3.1. Effect of the UIT on the surface microstructure of L-605 alloy

The optical micrograph of the annealed L-605 alloy is shown in Fig. 2(a), revealing a typical equiaxed grain structure. The corresponding X-ray diffraction (XRD) pattern of the annealed sample is presented in Fig. 2(b). Several distinct peaks appear at diffraction angles of approximately 44° , 51° , 75° , and 91° , corresponding to the (111), (200), (220), and (311) crystallographic planes, respectively. These peaks are indicative of a face-centered cubic (FCC) crystal structure and are

consistent with standard diffraction data for L-605 alloy reported in the literature [21].

The initial microstructure of the L-605 alloy consists of austenite matrix with a FCC crystal structure, featuring annealing twins (indicated by arrows in Fig. 2(a)). Image analysis revealed that the average grain size of the annealed sample is approximately $150 \pm 52 \mu\text{m}$. It is noteworthy that while the L-605 alloy possesses an FCC crystal structure at high temperatures and a hexagonal close-packed (HCP) at low temperatures, the FCC to HCP transformation during cooling is kinetically sluggish. As a result, the FCC phase remains quasi-stable in the alloy's microstructure after cooling.

Fig. 3(a-c) shows the cross-sectional microstructures of samples subjected to one, three and five passes of UIT, respectively.

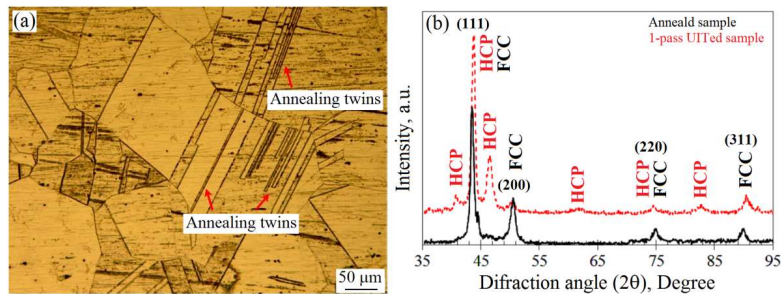


Fig. 2. (a) Optical micrograph showing the microstructure of the L-605 alloy in the annealed condition, and (b) corresponding X-ray diffraction (XRD) pattern confirming the FCC crystal structure.

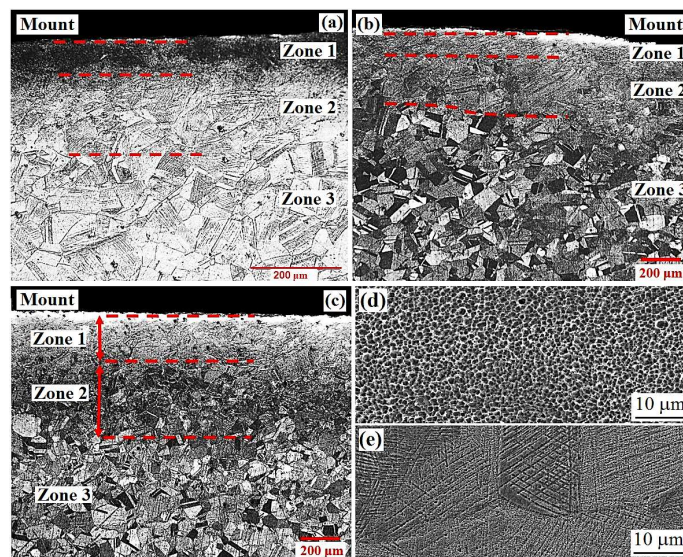


Fig. 3. (a-c) Optical micrographs of L-605 alloy after one, three, and five passes of UIT, respectively, (d, e) higher magnification FESEM images of the one-pass UITed sample showing the microstructures of zone 1 (severely plastically deformed, SPD layer) and zone 2 (plastically deformed, PD layer), respectively. Zone 3 corresponds to the undeformed base metal.

In all treated samples, two distinct regions are visible in the surface and near surface zones, and the thickness of these regions with the number of UIT passes. The microstructure of the one-pass UITed sample (Fig. 3(a)) exhibits a surface layer of severe plastic deformation (SPD) approximately 80 μm thick, followed by a plastically-deformed (PD) layer extending to a depth of about 180 μm . Increasing the UIT passes to three (Fig. 3(b)) results in a thicker SPD layer (120 μm) and PD layer (250 μm). In the five-pass UITed sample (Fig. 3(c)) the structural modification extends to a total depth exceeding 600 μm with two well-defined zones clearly distinguishable.

In the first zone (surface layer), SPD results in intense material flow, such that distinct grain boundaries are no longer visible. This observation is further confirmed by the high-magnification FESEM image of the SPD layer shown in Fig. 3(d). The microstructure of the PD layer, presented in Fig. 3(e), reveals a Widmanstätten-like structure characterized by a network of intersecting linear features. This is consistent with observations reported in previous studies [22, 23]. Transmission electron microscopy (TEM) analysis indicates that these Widmanstätten lines correspond to stacking faults, which appear as thin, planar defects in the structure band (Fig. 4(a)). Furthermore, the intersections of these stacking faults exhibit a locally disordered atomic arrangement, as clearly seen in Fig. 4(b). It is generally accepted that such intersecting features arise from the activation of secondary slip system, where dislocations interact with stacking fault planes or twin intersections, leading to the formation of

the observed network structure [7].

In Co-based alloys, the presence of striations is generally associated with the formation of ϵ -martensite phase [5]. Comparing the XRD patterns of the annealed and one-pass UITed samples (Fig. 2(b)) reveals the emergence of additional peaks at diffraction angles of approximately 41° , 47° , 62° , and 83° which correspond to an HCP phase. Concurrently, a reduction in the intensity of the original FCC peaks is observed. As a result, the structure of UITed samples consists of a mixture of FCC and HCP phases. This phase transformation is attributed to the strain-induced conversion of the FCC phase to HCP, suggesting that the UIT process promotes martensitic transformation. Knezevic et al. [24] have previously reported the intersection and merging of stacking faults as a mechanism for FCC-to-HCP transformation in the L-605 alloy. Similarly, Tawancy and colleagues [25] confirmed through TEM analysis, the formation of mechanical twins and HCP phase in L-605 alloy subjected to 20% cold work.

3.2. Effect of UIT on the surface microhardness of L-605 alloy

Fig. 5 presents the microhardness profiles measured at various depth beneath the surface of the UIT-processed L-605 alloy. For reference, the microhardness of the annealed sample is also included. It is evident that the application of UIT significantly increased the surface microhardness of the L-605 alloy and the microhardness remains 400 HV_{0.1} to a depth of approximately 700 μm below the treated surface.

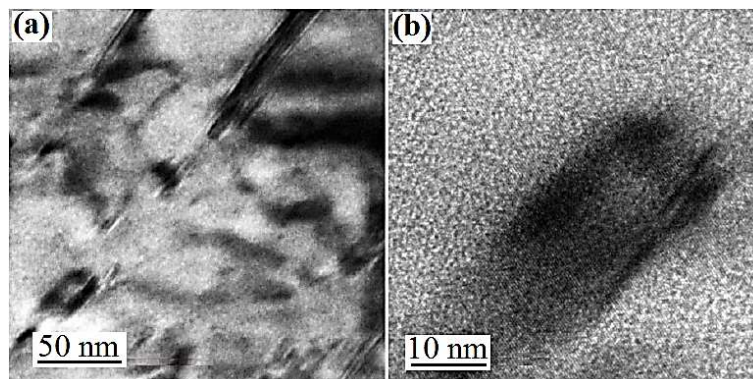


Fig. 4. TEM micrographs showing: (a) Widmanstätten lines and (b) stacking faults intersection.

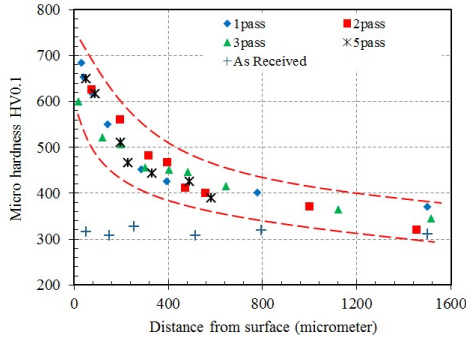


Fig. 5. In-depth microhardness profiles of the L-605 alloy in the annealed (as-received) and UITed conditions.

The improvement in surface microhardness of the UITed L-605 samples can be attributed to three primary mechanisms: work hardening (dislocation hardening), martensitic transformation, and grain refinement (Hall-Petch strengthening). Within the top $\sim 100 \mu\text{m}$ of the treated surface, the dominant hardening mechanisms are believed to be the formation of deformation twins and the intersection of stacking faults [5]. However, the accumulation of stacking faults and an increase in dislocation density appear to be the primary contributors to work hardening. Knezevic et al. reported that work hardening in L-605 alloy predominantly results from a density of stacking faults within grains and planar slip, without the formation of deformation twins. This behavior is attributed to the alloy's low stacking fault energy [2, 24] which increases the spacing between dislocation nucleation sites and hinders dislocation cross-slip and climb. In agreement with the XRD results (Fig. 2(b)), the formation of ultrafine grains (with a crystallite size of about 15 nm in the three-pass UITed sample) and the appearance of ϵ -martensite (HCP phase) also contribute significantly to the increased hardness. The semi-coherent interface of martensite plates acts as

strong barriers to dislocations motion, thus enhancing the overall strengthening effect [26].

Notably, the initial UIT passes (one and two) have the most pronounced effect on surface microhardness. However, further increasing the number of passes (up to five), shows a diminishing return, likely due to saturation of strain hardening in the surface layers. That is, while deeper layers continue to undergo deformation, the surface microhardness plateaus. As shown in previous studies [5], excessive strains accumulation can eventually exceed the fracture strain leading to the formation of surface microcracks.

3.3. Effect of UIT on the tribological properties of L-605 alloy

Fig. 6(a) shows the variation of wear rate for both annealed and UITed samples under different applied loads. Due to the formation of microcracks in the five-pass UITed sample, wear testing was not performed on this condition. As seen in Fig. 6(a), the wear rate of the annealed sample increases steadily with applied load, indicating a direct relationship between contact stress and material loss. In contrast, the specific wear rate (Fig. 6(b)) of the annealed sample shows a decreasing trend with increasing load, suggesting a shift in the wear mechanism. This behavior likely results from sliding-induced work hardening, which enhances the surface's resistance to further material removal under higher loads [24]. Regardless of the applied load, the first pass of the UIT significantly affects the wear behavior of the alloy. For any given applied load, the wear rate of the one-pass UITed sample is, on average, 70% lower than that of the annealed sample.

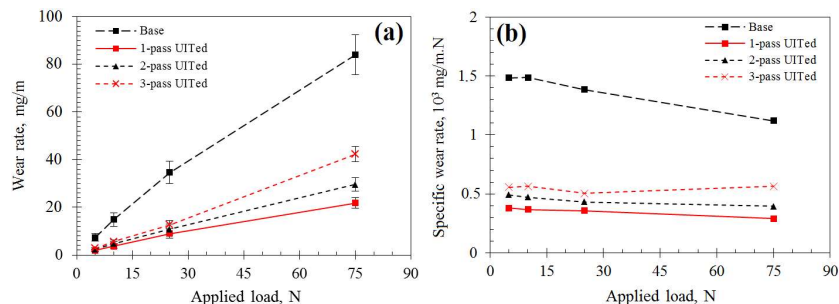


Fig. 6. Variation of (a) wear rate and (b) specific wear rate of the L-605 samples against the applied load.

However, increasing the number of UIT passes further negatively impacts wear resistance. Specifically, the wear rate of the three-pass UITed sample is about 81%, 66%, 58%, and 43% higher than that of the one-pass UITed sample under the applied loads of 5, 10, 25, and 75 N, respectively. This behavior aligns with the surface microhardness results.

The microscopic images of the worn surfaces of the annealed sample under the applied loads of 5, 25 and 75 N are presented in Fig. 7. Delaminated craters and abrasion grooves are clearly visible on the worn surface

of all samples. As the applied load increases, the extent of surface damages also increases. However, in line with the specific wear rate results (Fig. 6(b)), the amount of surface damages at 75 N is less than expected. This discrepancy is likely attributed to substrate work hardening. The EDS analysis of the worn surfaces is presented in Table 2 and Fig. 8. The presence of substantial oxygen in the worn surface composition suggests the formation of a tribolayer enriched with oxides.

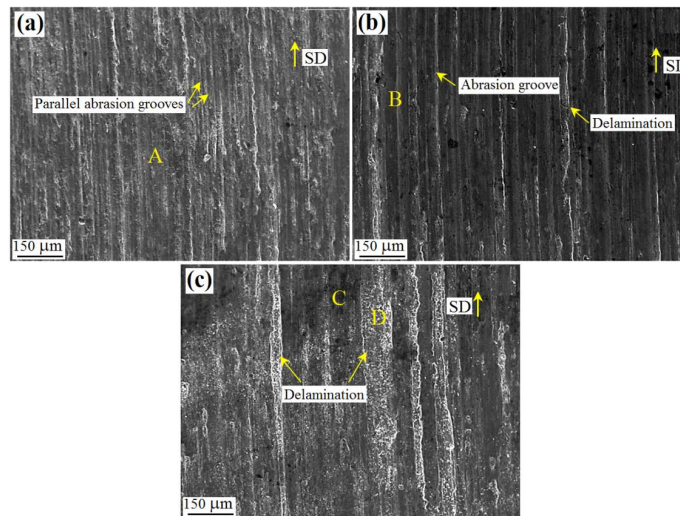


Fig. 7. SEM images of the worn surface of the annealed L-605 alloy after wear testing under applied loads of (a) 5 N, (b) 25 N, and (c) 75 N. The sliding direction (SD) is indicated by the arrow.

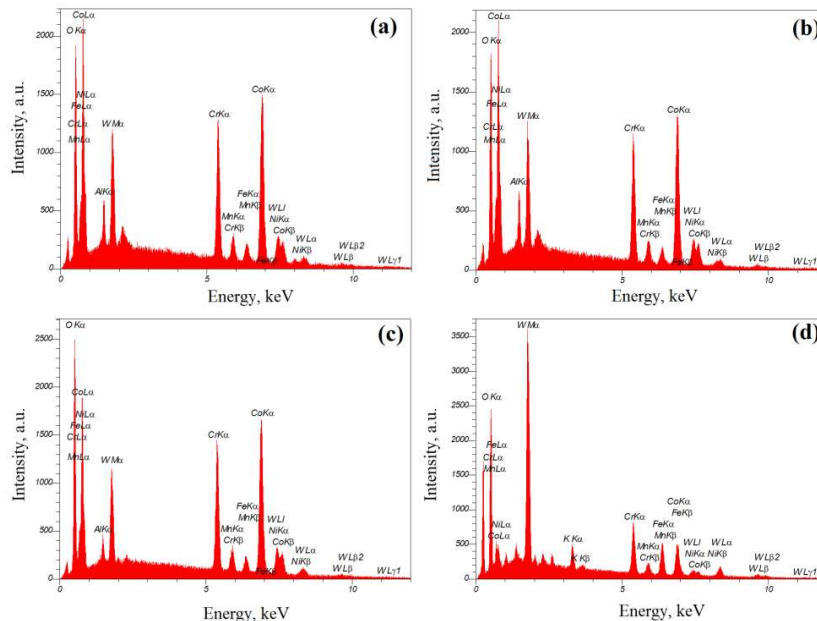


Fig. 8. EDS analyses of the marked areas in Fig. 7: (a) zone A, (b) zone B, (c) zone C, and (d) zone D.

Table 2. EDS analyses (in wt. %) of the different zones shown in Fig. 7

	O	Co	Cr	W	Ni	Al	Mn	Fe
Zone A	15.03	40.71	15.24	15.43	8.14	1.38	1.03	3.04
Zone B	19.59	38.07	14.28	18.78	7.89	1.79	0.94	2.68
Zone C	16.66	39.43	14.82	16.25	8.19	0.57	1.14	2.93
Zone D	24.11	12.23	9.48	39.74	2.33	1.94	1.10	9.08

During sliding wear, physicochemical processes such as mechanical mixing or alloying of transported materials (i.e., wear particles) and their chemical reactions with the environment result in the formation of a tribolayer, an oxide layer rich in oxygen [27, 28]. Additionally, the repeated stresses imposed on surfaces during sliding contacts can lead to "exo electron emission" releasing electrons from the surfaces and thereby promoting tribochemical reactions and oxide formation [29].

The mechanism of tribolayer and its decisive role in the tribological performance of engineering alloys have been extensively documented [28, 30]. Once formed, this layer protects the wear surface from direct contact and/or adhesion of asperities. Furthermore, due to its high oxide content and porous nature, the presence of a tribolayer can significantly reduce the material's coefficient of friction [31]. Its effectiveness, however, depends heavily on its physical and chemical properties, such as thickness, compactness, smoothness, and chemical composition [31].

A relatively thick, compact, and smooth oxide-rich tribolayer can significantly improve wear resistance. However, researchers have shown that the strength of the subsurface layers plays a crucial role in supporting this tribolayer, as the layer's mechanical integrity relies on that support [27, 31, 32]. The higher the resistance of the substrate to friction-induced strain, the more stable the tribolayer will be. Conversely, if the strength of the subsurface layers decreases due to factors such as elevated surface temperature, fracture of reinforcing phases, subsurface cracking, or phase transformations, the deformation in this region can compromise tribolayer stability, promoting its delamination. Therefore, the craters observed on the worn surface of the annealed sample likely indicate tribolayer delamination as one of the primary wear mechanisms in this alloy. These craters likely form due to the relatively low strength of the

substrate, which, under shear stresses from sliding wear, undergoes plastic deformation and loses its ability to support the tribolayer. Notably, tribolayer delamination begins with the nucleation of cracks in the subsurface area, typically within the tribolayer, and progressive via crack propagation parallel to the surface. These cracks are often initiated by stress concentration from friction-induced strains and tend to nucleate from defects such as porosities or weak interfaces around second phase particles embedded in the tribolayer. Increasing the applied load heightens the likelihood of crack initiation and propagation within the matrix. However, both prior studies and current findings indicate that while cracks may initiate, the tribolayer remains generally stable without complete delamination into the substrate. Instead, cracks often reach the surface and lead to the separation of material in the form of sheet-like particles [33].

In addition to the delaminated craters, numerous abrasion grooves are also evident on the worn surfaces. These are mainly from the result of three-body abrasion, caused by abrasive particles trapped between the sliding surfaces, or two-body abrasion, resulting from the interaction between the work-hardened asperities of the pin and hard asperities of the alumina disk [33]. Therefore, the dominant wear mechanisms in the annealed sample are abrasive wear and tribolayer delamination. According to the EDS analysis of points C and D in Figs. 7(c-d) and the corresponding data Table 2 and Fig. 8, even under high applied loads (75 N), delamination and abrasion remain largely confined to the tribolayer, with no evidence of severe wear or complete removal of the tribolayer from the surface.

The worn surface morphology of the one-pass UITED sample under the applied loads of 5, 25 and 75 N is shown in Fig. 9, and the corresponding EDS analyses of different surface regions are presented in Table 3. As shown, and consistent with the wear rate results in Fig.

6(a), the first pass of the UIT has significantly improved the surface quality of the pin, resulted in a well-compacted, protective and relatively smooth oxide-rich tribolayer. Regardless of the applied load, the amount of surface damage is considerably lower compared to the annealed sample (Fig. 7). Based on the worn surface morphology and EDS analyses (Table 3), the dominant wear mechanism of the one-pass UITed sample appear to be mild abrasive wear and slight delamination of the tribolayer. The positive impact of the UIT on the wear behavior of engineering alloys has been previously reported by other researchers. Another notable feature of the worn surface of the one-pass UITed sample is the low

concentration of Al in its tribolayer (Table 3 and Fig. 10), compared to the annealed sample (Table 2 and Fig. 8). The formation of the tribolayer is a dynamic process that begins with the onset of sliding and continues throughout the process. In other words, the tribolayer is constantly being formed and removed from the surface. Any factor that increases the rate of layer formation over enhances its stability, improving the wear properties. It appears that the increased substrate hardness of the one-pass UITed sample (Fig. 5) strengthens its ability to support the tribolayer, limiting the direct (destructive) contact between the sample's metallic surface and the alumina counterface.

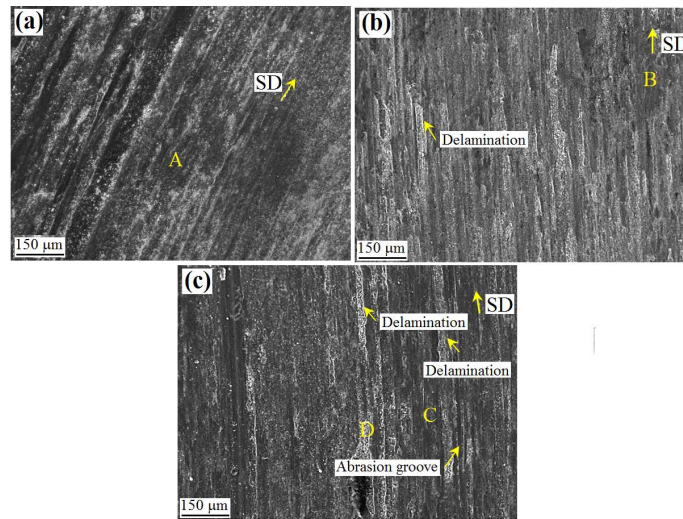


Fig. 9. SEM images showing the worn surfaces of one-pass UITed sample under applied loads of (a) 5 N, (b) 25 N, and (c) 75 N. The sliding direction is indicated by the arrow on the micrographs.

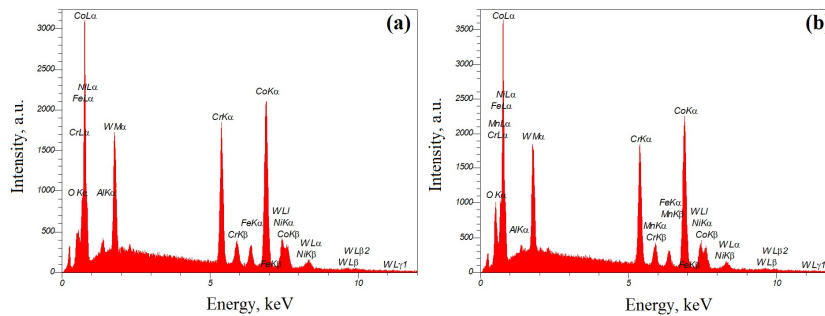


Fig. 10. EDS analysis of the marked areas on Fig. 9: (a) zone A and (b) zone B.

Table 3. EDS analyses of zones C and D shown on Fig. 9 (in wt. %)

	O	Co	Cr	W	Ni	Al	Mn	Fe
Zone C	28.19	32.39	16.08	9.75	6.26	0.17	3.03	4.13
Zone D	21.17	19.23	17.29	25.43	6.97	0.4	4.4	5.11

The positive impact of the first UIT pass on the wear properties of the L-605 alloy can be examined from several perspectives. As shown in Fig. 5, the first pass of UIT significantly increases surface hardness. Before the tribolayer forms (and separates the contacting surfaces) an increase in microhardness improves the asperities resistance to plastic deformation, reducing the likelihood of adhesion and junction growth at the contact points. This decreases the adhesion component of the friction and, consequently, the growth of surface temperature minimizing the substrate thermal softening (and its subsequent consequences). After the formation of the tribolayer, increasing the substrate hardness (or equivalently increasing its resistance against the plastic deformation) improves the tribolayer stability thereby increases the wear resistance.

Investigating the variation of the wear rate against the Vickers microhardness, nanohardness, elastic index (elastic strain to fracture), and plastic index (material resistance to plastic deformation) at the different applied loads (Figs. 11(a) to 11(c)) also depicts the good relationship between the observed trend in the alloy wear and the strength parameters of the material. The parameter H/E_r indicates the resistance of the material against the wear damage (the wear resistance of a material is also related to its resistance to elastic strain at the nano scale fracture) and H^3/E_r^2 refers to the material

ability to resist the wear phenomenon [34, 35]. These parameters are widely used to define the wear resistance of materials [34-36]. As observed, after a significant increase in the wear resistance of the one-pass UITed sample, the onset of hardness saturation and/or the formation of surface microcracks likely destabilizes the tribolayer, negatively affecting the wear resistance of the two-, three- and five-pass UITed samples.

The effect of the UIT on the average friction coefficient (AFC) of L-605 alloy in sliding wear under the different applied loads (5, 10, 25 and 75 N) is shown in Fig. 12. As can be seen, regardless of the applied load, performing the UIT up to one pass causes a significant reduction in the AFC. Under the applied loads of 10 and 75 N, the AFC of one-pass UITed sample decreases by about 80 and 74 %, respectively. However, a further increase in the number of UIT passes causes an increase in the AFC. In addition, the higher the applied load is, the higher the AFC value which can be attributed to the enhancement of the two adhesive components and the plastic deformation (abrasion) of the friction coefficient. Therefore, a good conformance exists between the friction and wear properties of the alloy. The variations of the friction coefficient of the annealed and one-pass UITed samples as a function of the sliding distance at the applied loads of 10, 25, and 75 N are shown in Fig. 13.

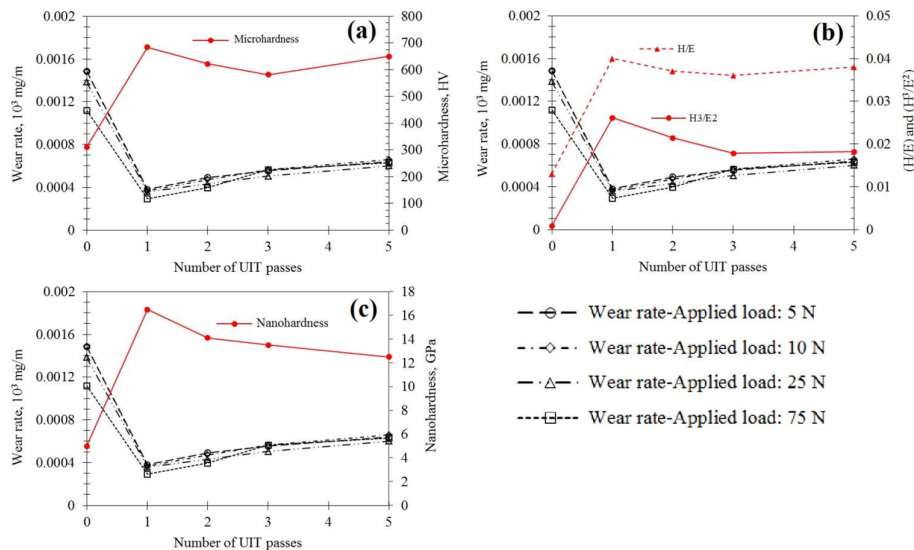


Fig. 11. Variation of the wear rate of annealed and UITed samples against the number of passes and different applied loads compared to (a) the alloy microhardness, (b) the plasticity index/elasticity index parameters, and (c) the alloy nanohardness.

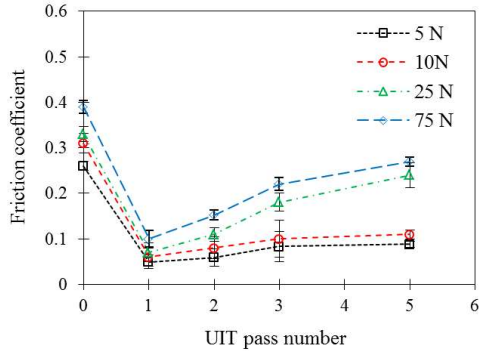


Fig. 12. Friction coefficient diagrams of the annealed and UITed samples against pass number.

As seen, after an initial running-in stage in which the friction coefficient increases suddenly, the friction coefficient of all samples enters a steady state phase. The emergence of the running-in period is attributed to the interaction of surface asperities, junction growth (increasing the real contact area), three-body abrasive wear caused by the interaction of abrasive particles between the sliding surfaces, and work hardening of the surfaces [37, 38].

After passing the running-in, the alloys show a more stable frictional behavior. The friction coefficient of the annealed sample is higher than 0.3 (at the three examined loads). The amplitude of the friction coefficient fluctuations is also significant. Energy-intensive processes like tribolayer delamination and plastic deformation (surface ploughing due to two- or three-body wear or sub-layer flow) primarily regulate the

steady-state sliding friction behavior, nucleation and propagation of surface/sub-surface microcracks, fragmentation of sub-surface phases, etc. Accordingly, at a given applied load, the fluctuations in the friction coefficient and the higher friction coefficient of the annealed alloy can be attributed to the relative instability of the tribolayer formed on its wear surface (Fig. 7).

Applying the UIT in the first pass causes a significant reduction in the friction coefficient and the amplitude of its fluctuations (Figs. 13(d-f)) which is probably related to the presence of a stable and protective tribolayer on the wear surface (Fig. 9) whose presence, on the one hand, reduces the possibility of direct contact (adhesive wear) between the surface asperities and, on the other hand, reduces the shear strength of the friction pair interface according to the Eq. (1) [2]:

$$\mu = \frac{1}{\sqrt{\alpha \left[\left(\frac{\tau_o}{\tau_i} \right)^2 - 1 \right]}} \quad (1)$$

Where μ is the coefficient of friction, α is a constant, and τ_o and τ_i are the bulk and interface shear strengths, respectively. It is evident that the tribolayer shear strength (τ_i) and the friction coefficient are inversely related. Thus, tribolayer creation is probably going to lower the AFC.

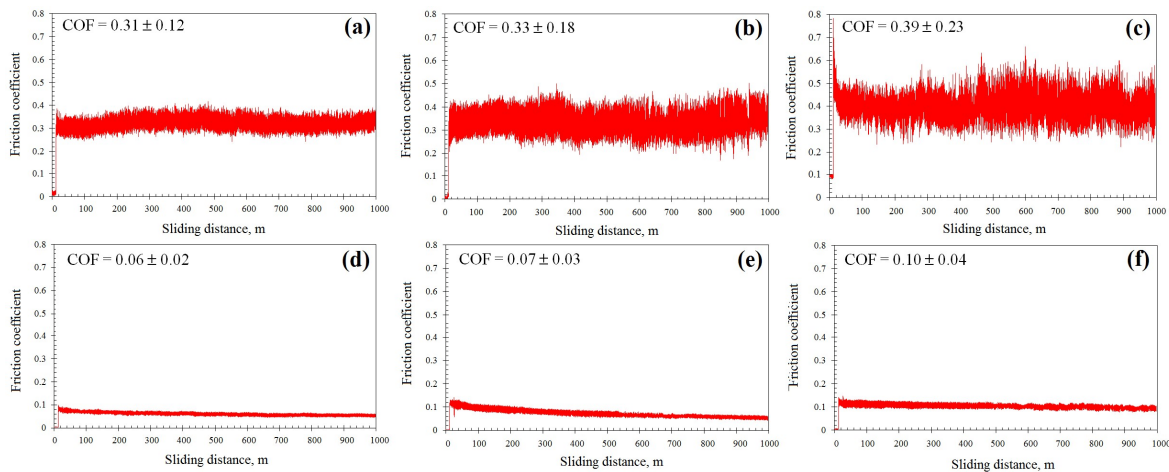


Fig. 13. Friction coefficient diagrams of the annealed sample (a) 10 N, (b) 25 N, (c) 75 N, and the one-pass UITed sample (d) 10 N, (e) 25 N, and (f) 75 N.

4. Conclusions

- 1) Application of ultrasonic impact treatment (UIT) significantly deforms the surface regions of the L-605 alloy up to a depth of approximately 600 μm (after five passes). In addition, UIT induces a phase transformation in the alloy's crystal structure from FCC (austenite) to HCP (ϵ -martensite).
- 2) UIT increases the surface microhardness of the L-605 alloy from 315 HV to over 630 HV within the top 50 μm . Moreover, hardness values exceeding 400 HV are recorded up to a depth of approximately 700 μm . Although microhardness improves with increasing passes, the rate of strain accumulation, eventually reaching a saturation point.
- 3) UIT enhances the wear resistance of L605 alloy. Under applied loads of 5, 10, 25 and 75 N, the wear rate of the one-pass UITed sample is, on average, about 70 % lower than that of the annealed alloy. Furthermore, UIT process reduces the friction coefficients of samples indicate that UIT reduces the friction coefficient by up to 50 %, lowering it from 0.34 in the annealed state to approximately 0.17-0.23 in UITed samples.
- 4) While the first UIT pass substantially improves wear resistance, subsequent passes (two, three, and five) may lead to hardness saturation and/or surface microcrack formation. These factors could destabilize the tribolayer and negatively impact wear resistance.
- 5) Localized surface enhancement of annealed L-605 biomedical components via UIT, a cost-effective, simple, and efficient severe surface plastic deformation (S^2PD) technique, can significantly reduce implant wear and improve their longevity in biomedical applications, while also minimizing manufacturing costs.

Conflict of interest

The author declares that there is no conflict of interest related to this research.

Funding

This research has not received any specific grant or

funding from public, commercial, or not-for-profit sectors.

Author Contributions

Rahim Nemati: Software, Investigation, Validation, Formal analysis; Writing-Original Draft

Reza Taghiabadi: Conceptualization, Methodology, Project administration, Validation, Writing-Review & Editing

Morteza Saghafi Yazdi: Conceptualization, Methodology, Project administration, Validation

Saeid Amini: Project administration, Methodology

5. References

- [1] Crook, P. (1990). Cobalt and cobalt alloys, *ASM Handbook, properties selection of nonferrous alloy and special-purpose material*. ASM International, USA.
- [2] Nemati, R., Taghiabadi, R., Saghafi Yazdi, M., & Amini, S. (2023). Effect of severe surface plastic deformation on tribological properties of CoCrWNi super alloys. *Iranian Journal of Materials Forming*, 10(2), 22-34. <https://doi.org/10.22099/IJMF.2023.47206.1256>
- [3] Sharath Kumar, J., Kumar, R., & Verma, R. (2024). Surface modification aspects for improving biomedical properties in implants: A review. *Acta Metallurgica Sinica (English Letters)*, 37(2), 213-241. <https://doi.org/10.1007/s40195-023-01631-7>
- [4] Diaz-Rodriguez, S., Chevallier, P., Paternoster, C., Montañó-Machado, V., Noël, C., Houssiau, L., & Mantovani, D. (2019). Surface modification and direct plasma amination of L605 CoCr alloys: on the optimization of the oxide layer for application in cardiovascular implants. *RSC Advances*, 9(4), 2292-2301. <https://doi.org/10.1039/C8RA08541B>
- [5] Nemati, R., Taghiabadi, R., Yazdi, M. S., & Amini, S. (2025). Ultrasonic impact treatment of CoCrWNi superalloys for surface properties improvement. *Materials Testing*, (2), 372-385. <https://doi.org/10.1515/mt-2024-0134>
- [6] Schulze V., (2006). *Modern mechanical surface treatment: states, stability, effects*. John Wiley & Sons.
- [7] López de Lacalle, L. N., Lamikiz, A., Sánchez, J. A., & Arana, J. L. (2007). The effect of ball burnishing on heat-treated steel and Inconel 718 milled surfaces. *The International Journal of Advanced Manufacturing Technology*, 32, 958-968. <https://doi.org/10.1007/s00170-005-0402-5>
- [8] Acharya, S., Suwas, S., & Chatterjee, K. (2021). Review of recent developments in surface nanocrystallization of

- metallic biomaterials. *Nanoscale*, 13(4), 2286-2301. <https://doi.org/10.1039/D0NR07566C>
- [9] Abdollahi, A., Honarpisheh, M., & Amini, S. (2024). Experimental study of the effects of the ultrasonic peening treatment on surface hardness and hardness depth of wire EDMed workpieces. *Iranian Journal of Materials Forming*, 11(1), 44-61. <https://doi.org/10.22099/IJMF.2024.49938.1290>
- [10] Omid Hashjin, A., Vahdati, M., & Abedini, R. (2024). Investigating the effect of ultrasonic shot peening parameters on metallurgical, mechanical, and corrosion properties of industrial parts: A literature review. *Iranian Journal of Materials Forming*, 11(2) 75-95. <https://doi.org/10.22099/IJMF.2024.50081.1294>
- [11] Sebdani, R. M., Bilan, H. K., Gale, J. D., Wann, J., Madireddy, G., Sealy, M. P., & Achuthan, A. (2024). Ultrasonic impact treatment (UIT) combined with powder bed fusion (PBF) process for precipitation hardened martensitic steels. *Additive Manufacturing*, 84, 104078. <https://doi.org/10.1016/j.addma.2024.104078>
- [12] Ansarian, I., Taghiabadi, R., Amini, S., Mosallanejad, M. H., Iuliano, L., & Saboori, A. (2024). Improvement of surface mechanical and tribological characteristics of L-PBF processed commercially pure titanium through ultrasonic impact treatment. *Acta Metallurgica Sinica (English Letters)*, 1-13. <https://doi.org/10.1007/s40195-024-01696-y>
- [13] Karimi, A., & Amini, S. (2016). Steel 7225 surface ultrafine structure and improvement of its mechanical properties using surface nanocrystallization technology by ultrasonic impact. *The International Journal of Advanced Manufacturing Technology*, 83, 1127-1134. <https://doi.org/10.1007/s00170-015-7619-8>
- [14] Luna-Manuel, J. C., Lagar-Quinto, S., Ramirez-Ledesma, A. L., & Juarez-Islas, J. A. (2021). Thermomechanical and annealing processing effect on a rapid solidified Co-20 wt.% Cr alloy. *Journal of Physics: Conference Series* (Vol. 1723, No. 1, p. 012002). IOP Publishing. <https://doi.org/10.1088/1742-6596/1723/1/012002>
- [15] Lesyk, D. A., Martinez, S., Mordiyuk, B. N., Dzhemelinskiy, V. V., Lamikiz, A., & Prokopenko, G. I. (2020). Post-processing of the Inconel 718 alloy parts fabricated by selective laser melting: Effects of mechanical surface treatments on surface topography, porosity, hardness and residual stress. *Surface and Coatings Technology*, 381, 125136. <https://doi.org/10.1016/j.surfcoat.2019.125136>
- [16] Panin, A. V., Kazachenok, M. S., Kozelskaya, A. I., Balokhonov, R. R., Romanova, V. A., Perevalova, O. B., & Pochivalov, Y. I. (2017). The effect of ultrasonic impact treatment on the deformation behavior of commercially pure titanium under uniaxial tension. *Materials & Design*, 117, 371-381. <https://doi.org/10.1016/j.matdes.2017.01.006>
- [17] Wang, Z., Liu, Z., Gao, C., Wong, K., Ye, S., & Xiao, Z. (2020). Modified wear behavior of selective laser melted Ti6Al4V alloy by direct current assisted ultrasonic surface rolling process. *Surface and Coatings Technology*, 381, 125122. <https://doi.org/10.1016/j.surfcoat.2019.125122>
- [18] Amanov, A., Lee, S. W., & Pyun, Y. S. (2017). Low friction and high strength of 316L stainless steel tubing for biomedical applications. *Materials Science and Engineering: C*, 71, 176-185. <https://doi.org/10.1016/j.msec.2016.10.005>
- [19] Amanov, A. (2021). Effect of post-additive manufacturing surface modification temperature on the tribological and tribocorrosion properties of Co-Cr-Mo alloy for biomedical applications. *Surface and Coatings Technology*, 421, 127378. <https://doi.org/10.1016/j.surfcoat.2021.127378>
- [20] Abbasi, A., Amini, S., & Sheikhzadeh, G. A. (2018). Effect of ultrasonic peening technology on the thermal fatigue of rolling mill rolls. *The International Journal of Advanced Manufacturing Technology*, 94, 2499-2513. <https://doi.org/10.1007/s00170-017-0840-x>
- [21] Wang, R., Chen, D., Qin, G., & Zhang, E. (2020) Novel CoCrWNi alloys with Cu addition: Microstructure, mechanical properties, corrosion properties and biocompatibility. *Journal of Alloys and Compounds*, 824(25), 153924. <https://doi.org/10.1016/j.jallcom.2020.153924>
- [22] Yamanaka, K., Mori, M., & Chiba, A. (2012). Origin of significant grain refinement in Co-Cr-Mo alloys without severe plastic deformation. *Metallurgical and Materials Transactions A*, 43, 4875-4887. <https://doi.org/10.1007/s11661-012-1303-5>
- [23] Luo, J., Wu, S., Lu, Y., Guo, S., Yang, Y., Zhao, C., & Lin, J. (2018). The effect of 3 wt.% Cu addition on the microstructure, tribological property and corrosion resistance of CoCrW alloys fabricated by selective laser melting. *Journal of Materials Science: Materials in Medicine*, 29, 1-16. <https://doi.org/10.1007/s10856-018-6043-7>
- [24] Knezevic, M., Carpenter, J. S., Lovato, M. L., & McCabe, R. J. (2014). Deformation behavior of the cobalt-based superalloy Haynes 25: Experimental characterization and crystal plasticity modeling. *Acta Materialia*, 63, 162-168. <https://doi.org/10.1016/j.actamat.2013.10.021>
- [25] Tawancy, H. M., Ishwar, V. R., & Lewis, B. E. (1986). On the fcc→hcp transformation in a cobalt-base superalloy (Haynes alloy No. 25). *Journal of Materials Science Letters*, 5(3), 337-341. <https://doi.org/10.1007/BF01748098>

- [26] Lee, B. S., Matsumoto, H., & Chiba, A. (2011). Fractures in tensile deformation of biomedical Co–Cr–Mo–N alloys. *Materials Letters*, 65(5), 843-846. <https://doi.org/10.1016/j.matlet.2010.12.007>
- [27] Akbari, F., Golkaram, M., Beyrami, S., Shirazi, G., Mantashloo, K., Taghiabadi, R., & Ansarian, I. (2024). Effect of solidification cooling rate on microstructure and tribology characteristics of Zn-4Si alloy. *International Journal of Minerals, Metallurgy and Materials*, 31(2), 362-373. <https://doi.org/10.1007/s12613-023-2764-9>
- [28] Lu, Z. C., Zeng, M. Q., Gao, Y., & Zhu, M. (2013). Minimizing tribolayer damage by strength–ductility matching in dual-scale structured Al–Sn alloys: a mechanism for improving wear performance. *Wear*, 304(1-2), 162-172. <https://doi.org/10.1016/j.wear.2013.05.001>
- [29] Tran, B. H., Tieu, A. K., Wan, S., Zhu, H., Mitchell, D. R., & Nancarrow, M. J. (2017). Multifunctional bilayered tribofilm generated on steel contact interfaces under high-temperature melt lubrication. *The Journal of Physical Chemistry C*, 121(45), 25092-25103. <https://doi.org/10.1021/acs.jpcc.7b06874>
- [30] Nouri, Z., & Taghiabadi, R. (2021). Tribological properties improvement of conventionally-cast Al-8.5Fe-1.3V-1.7Si alloy by multi-pass friction stir processing. *Transactions of Nonferrous Metals Society of China*, 31(5), 1262-1275. [https://doi.org/10.1016/S1003-6326\(21\)65576-0](https://doi.org/10.1016/S1003-6326(21)65576-0)
- [31] Ashoori, M., Jafarzadegan, M., Taghiabadi, R., Saghafi Yazdi, M., & Ansarian, I. (2023). Enhancing the tribological properties of pure Ti by pinless friction surface stirring. *Materials Science and Technology*, 39(18), 3308-3320. <https://doi.org/10.1080/02670836.2023.2249749>
- [32] Moharrami, A., Razaghian, A., Paidar, M., Šlapáková, M., Ojo, O. O., & Taghiabadi, R. (2020). Enhancing the mechanical and tribological properties of Mg₂Si-rich aluminum alloys by multi-pass friction stir processing. *Materials Chemistry and Physics*, 250, 123066. <https://doi.org/10.1016/j.matchemphys.2020.123066>
- [33] Hutchings I., & Shipway P. (2017). *Tribology: friction and wear of engineering materials*. Butterworth-Heinemann.
- [34] Atace, A., Li, Y., & Wen, C. (2019). A comparative study on the nanoindentation behavior, wear resistance and in vitro biocompatibility of SLM manufactured CP–Ti and EBM manufactured Ti64 gyroid scaffolds. *Acta Biomaterialia*, 97, 587-596. <https://doi.org/10.1016/j.actbio.2019.08.008>
- [35] Attar, H., Ehtemam-Haghighi, S., Kent, D., Okulov, I. V., Wendrock, H., Bönisch, M., & Dargusch, M. S. (2017). Nanoindentation and wear properties of Ti and Ti–TiB composite materials produced by selective laser melting. *Materials Science and Engineering: A*, 688, 20-26. <https://doi.org/10.1016/j.msea.2017.01.096>
- [36] Shahriyari, F., Taghiabadi, R., Razaghian, A., & Mahmoudi, M. (2018). Effect of friction hardening on the surface mechanical properties and tribological behavior of biocompatible Ti-6Al-4V alloy. *Journal of Manufacturing Processes*, 31, 776-786. <https://doi.org/10.1016/j.jmapro.2017.12.016>
- [37] Sarmadi, H., Kokabi, A. H., & Reihani, S. S. (2013). Friction and wear performance of copper–graphite surface composites fabricated by friction stir processing (FSP). *Wear*, 304(1-2), 1-12. <https://doi.org/10.1016/j.wear.2013.04.023>
- [38] Samuel, C., Arivarasu, M., & Prabhu, T. R. (2020). High temperature dry sliding wear behaviour of laser powder bed fused Inconel 718. *Additive Manufacturing*, 34, 101279. <https://doi.org/10.1016/j.addma.2020.101279>